

1 **Rheologic constraints on the upper mantle from five years of**
2 **postseismic deformation following the El Mayor-Cucapah**
3 **earthquake**

4 **T. T. Hines¹, E. A. Hetland¹**

5 ¹Department of Earth and Environmental Sciences, University of Michigan, Ann Arbor, Michigan, USA.

6 **Key Points:**

- 7 • = enter point 1 here =
8 • = enter point 2 here =
9 • = enter point 3 here =

10 **Abstract**

11 Five years of postseismic deformation following the Mw7.2 El Mayor-Cucapah earthquake re-
 12 veals transient deformation that decays back to its pre-earthquake trend after about three years
 13 at epicentral distances greater than ~ 200 km. At closer distances, the rapid transience decays
 14 to a sustained rate which exceeds its pre-earthquake trend. We attempt to determine the mech-
 15 anisms driving this deformation, where we consider afterslip at seismogenic depths and vis-
 16 coelastic relaxation in the lower crust and upper mantle as candidate mechanisms. We find that
 17 early, rapid, near-field deformation can be explained with afterslip on the fault that ruptured
 18 coseismically, while the later, sustained, near-field deformation can be explained with either
 19 continued afterslip in an effectively elastic lower crust, or lower crustal viscoelastic relaxation
 20 with a steady-state viscosity of $\sim 10^{19}$ Pa s. The trend in far-field deformation is best explained
 21 with a transient viscosity of $\sim 10^{18}$ Pa s in the upper mantle. We argue that a transient rhe-
 22 ology in the mantle is preferable over a Maxwell rheology because it better predicts the de-
 23 cay in postseismic deformation, and also because it does not conflict with the generally higher,
 24 steady-state viscosities inferred from studies of geophysical processes occurring over longer
 25 time-scales.

26 **1 Introduction**

27 Ground deformation in the years following a large (\gtrsim Mw7) earthquake provides insight
 28 into the mechanical behavior of the crust and upper mantle. It has long been recognized that
 29 interpretations of postseismic deformation can be ambiguous because multiple postseismic de-
 30 formation mechanisms can have qualitatively similar surface expressions [e.g. Savage, 1990].
 31 Owing to the dense geodetic network deployed throughout the 2000s as part of the Plate Bound-
 32 ary Observatory, the postseismic deformation following the April 4, 2010, Mw7.2 El Mayor-
 33 Cucapah earthquake in Baja California was observed at more GPS stations than any other earth-
 34 quake in California to date. With such a large collection of data, we attempt to discern the mech-
 35 anisms driving postseismic deformation following the El Mayor-Cucapah earthquake, where
 36 we consider both afterslip and viscoelastic relaxation in the lower crust and upper mantle as
 37 candidate mechanisms.

38 Previous studies which have modeled postseismic deformation following the El Mayor-
 39 Cucapah earthquake include Pollitz *et al.* [2012], Gonzalez-Ortega *et al.* [2014], Spinler *et al.*
 40 [2015], and Rollins *et al.* [2015]. Of these studies, Gonzalez-Ortega *et al.* [2014] and Rollins
 41 *et al.* [2015] have attempted to describe the postseismic deformation with afterslip in an elas-
 42 tic half-space. Gonzalez-Ortega *et al.* [2014] described five months of postseismic deforma-
 43 tion, observed by InSAR and GPS within ~ 50 km of the rupture, with afterslip and contrac-
 44 tion on the coseismically ruptured fault. Gonzalez-Ortega *et al.* [2014] noted that their preferred
 45 model underestimated the GPS displacements for stations $\gtrsim 25$ km from the rupture and sug-
 46 gested that it could be the result of unmodeled viscoelastic relaxation. Using only continuous
 47 GPS stations, which are mostly north of the rupture zone, Rollins *et al.* [2015] found that three
 48 years of postseismic deformation can be adequately explained by afterslip, albeit with an im-
 49 plausibly large amount of slip inferred on the least constrained, southern-most fault segment.
 50 Here, we suggest the afterslip inferred by Rollins *et al.* [2015] may have been acting as a proxy
 51 for distributed relaxation in the upper mantle.

52 Pollitz *et al.* [2012], Rollins *et al.* [2015] and Spinler *et al.* [2015] have explored viscoelas-
 53 tic relaxation in the lower crust and upper mantle as a potential postseismic deformation mech-
 54 anism. The rheology of the crust and mantle is largely unknown and so modeling postseis-
 55 mic deformation with viscoelastic relaxation requires one to assume a rheologic model and
 56 then find the best fitting rheologic parameters. The inference of these rheologic parameters is
 57 a computationally expensive non-linear inverse problem which is typically approached with
 58 a forward modeling grid search method. Consequently, a simplified structure for the Earth must
 59 be assumed in order to minimize the number of rheologic parameters that need to be estimated.
 60 For example, it is commonly assumed that the lower crust and upper mantle are homogeneous,

Maxwell viscoelastic layers, which may be too simplistic for postseismic studies [Riva and Govers, 2009; Hines and Hetland, 2013]. To further reduce the dimensions of the model space, it is also necessary to make simplifying assumptions about the nature of afterslip. For example, one can assume a frictional model for afterslip and parametrize afterslip in terms of the unknown rheologic properties of the fault [e.g. Johnson *et al.*, 2009; Johnson and Segall, 2004]. One can also assume that afterslip does not persist for more than a few months and then model the later postseismic deformation assuming it to be the result of only viscoelastic relaxation [e.g. Pollitz *et al.*, 2012; Spinler *et al.*, 2015]. However, postseismic afterslip in similar tectonic settings has been observed to persist for decades following earthquakes [Çakir *et al.*, 2012; Cetin *et al.*, 2014]. Indeed, the preferred viscoelastic model from Pollitz *et al.* [2012] significantly underestimates deformation in the Imperial Valley, which could be indicative of unmodeled continued afterslip. Neglecting to allow for sustained afterslip as a postseismic mechanism could then lead to biased inferences of viscosities.

In this study, we perform a kinematic inversion for fault slip, allowing it to persist throughout the postseismic period, while simultaneously estimating the viscosity of the lower crust and upper mantle. We use the method described in Hines and Hetland [2016] to create an initial model of the fault slip and effective viscosity necessary to describe early postseismic deformation, which has the richest signature of the underlying deformation mechanisms. Our initial model describes the first 0.8 years of postseismic deformation following the El Mayor-Cucapah earthquake. We then use the inferred effective viscosity structure from the initial model to create a suite of postseismic models to explain the five years of postseismic data available to date. Of the suite of models tested, we find that postseismic deformation following the El Mayor-Cucapah earthquake can be explained with a combination of afterslip on a fault segment running through the Sierra Cucapah, a Zener rheology in the upper mantle with a transient viscosity that decays from 6×10^{18} Pa s to 1×10^{18} Pa s at 120 km depth, and a relatively stronger lower crust.

2 Data Processing

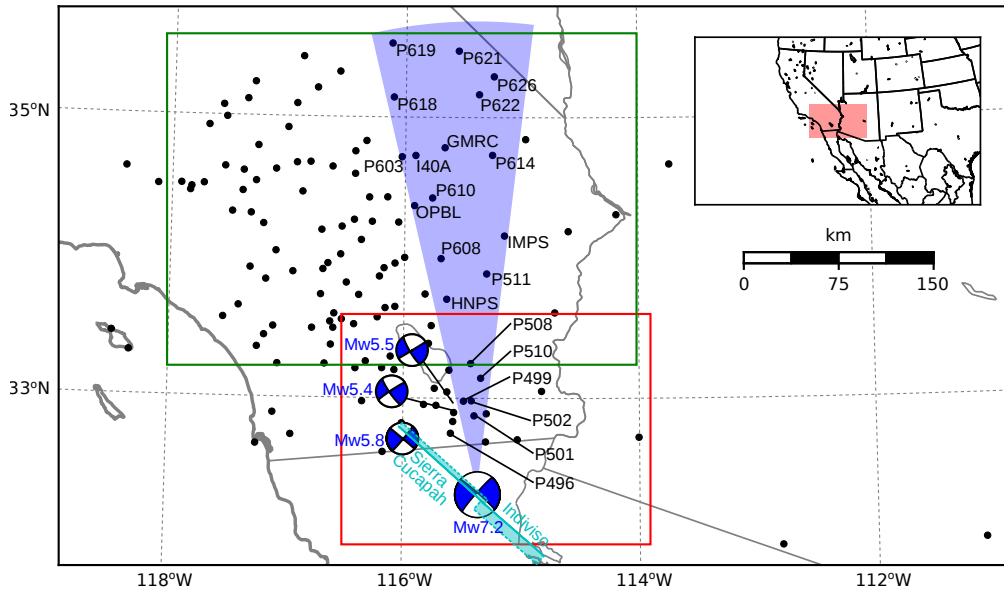
We use continuous GPS position time series provided by University Navstar Consortium (UNAVCO) for stations within a 400 km radius about the El Mayor-Cucapah epicenter. We collectively describe the coseismic and postseismic displacements resulting from the El Mayor-Cucapah earthquake as $u_{\text{post}}(t)$. We consider the GPS position time series $u_{\text{obs}}(t)$ to be the combination of $u_{\text{post}}(t)$, secular tectonic deformation, annual and semi-annual oscillations, and coseismic offsets from significant earthquakes over the time span of this study. The June 14, 2010, Mw5.8 Ocotillo earthquake and the Brawley swarm, which included an Mw5.5 and an Mw5.4 event on August 26, 2012, (Figure 1) are the only earthquakes that produced noticeable displacements in any of the time series. We treat the displacements resulting from the Brawley swarm as a single event because the daily solutions provided by UNAVCO cannot resolve the separate events. Although the Ocotillo earthquake had its own series of aftershocks [Hauksson *et al.*, 2011], neither the Ocotillo earthquake nor the Brawley swarm produced detectable postseismic deformation. We model displacements resulting from these events with only a Heaviside function, $H(t)$, describing the coseismic offsets. We then model $u_{\text{obs}}(t)$ as

$$u_{\text{obs}}(t) = u_{\text{pred}}(t) + \epsilon, \quad (1)$$

where

$$\begin{aligned} u_{\text{pred}}(t) = & u_{\text{post}}(t)H(t - t_{\text{emc}}) + c_0 + c_1 t + \\ & c_2 \sin(2\pi t) + c_3 \cos(2\pi t) + c_4 \sin(4\pi t) + c_5 \cos(4\pi t) + \\ & c_6 H(t - t_{\text{oc}}) + c_7 H(t - t_{\text{bs}}). \end{aligned} \quad (2)$$

In the above equations, t_{emc} , t_{oc} and t_{bs} are the times of the El Mayor-Cucapah earthquake, Ocotillo earthquake, and the Brawley swarm, respectively, c_0 through c_7 are unknown coefficients, and ϵ is the observation noise. We only estimate jumps associated with the Ocotillo earthquake and Brawley swarm for stations within 40 km of their epicenters.



87 **Figure 1.** Map of the region considered in this study. The large focal mechanism is for the El Mayor-
 88 Cucapah earthquake, and the three small focal mechanisms are for the Ocotillo earthquake and the two main
 89 shocks during the Brawley swarm. The black dots indicate the locations of GPS stations used in this study.
 90 The fault geometry used in this study is shown in cyan where dashed lines indicate buried edges of the fault
 91 segments. The green and red boxes demarcate the extent of the near-field and far-field maps (Figures 4 and 5).
 92 Stations inside the blue sector, which highlights the area within 10° of the El Mayor-Cucapah P axis, are used
 93 in Figures 7, 10, and 14

99 Stations which recorded displacements that clearly cannot be described by the aforementioned
 100 processes are not included in our analysis. This includes stations in the Los Angeles
 101 basin, where anthropogenic deformation can be larger than the postseismic signal that we are
 102 trying to estimate [Bawden *et al.*, 2001; Argus *et al.*, 2005]. In order to ensure an accurate es-
 103 timation of the secular deformation, we only use stations that were installed at least six months
 104 prior to El Mayor-Cucapah earthquake. Several GPS stations were installed after the El Mayor-
 105 Cucapah earthquake to improve the spatial resolution of postseismic deformation [Spinler *et al.*,
 106 2015]. Although it would be possible to subtract secular velocities derived from elastic block
 107 models [e.g. Meade and Hager, 2005] from velocities recorded at the newly installed stations
 108 to get an estimate of postseismic velocities, we do not do so here. We use coseismic and post-
 109 seismic displacements, rather than velocities, in our inverse method described in Section 3. We
 110 use displacements because estimating velocities from an already noisy displacement time se-
 111 ries can introduce significant uncertainties depending on exactly how the estimation is done.
 112 This choice prevents us from using the newly installed stations in Baja California for our anal-
 113 ysis.

114 The October 16, 1999, Mw7.1 Hector Mine earthquake, which occurred \sim 270 km north
 115 of the El Mayor-Cucapah epicenter, produced transient postseismic deformation which we do
 116 not wish to model, either mechanically or through empirical line fitting. We thus restrict our
 117 analysis to deformation observed six years after the Hector Mine earthquake, which is when
 118 postseismic velocities at sites proximal to the Hector Mine epicenter are approximately con-
 119 stant [Savage and Svare, 2009]. When appraising our model fit in Section 3, we see some sys-
 120 tematic residuals in the vicinity of the Hector Mine epicenter, which may be the result of er-
 121 rors in the assumption that the trend in Hector Mine postseismic deformation is linear after
 122 six years.

Studies of postseismic deformation typically assume a parametric form for $u_{\text{post}}(t)$, such as one with a logarithmic or exponential time dependence [e.g. Savage *et al.*, 2005]. However, by assuming a logarithmic or exponential form of $u_{\text{post}}(t)$ we run the risk of over fitting the GPS time series and inferring a non-existent postseismic signal. We therefore do not assume any parametric form for $u_{\text{post}}(t)$ and rather treat it as integrated Brownian motion, so that

$$\dot{u}_{\text{post}}(t) = \sigma^2 \int_0^t w(s) ds, \quad (3)$$

where $w(t)$ is white noise and the variance of $\dot{u}_{\text{post}}(t)$ increases linearly with time by a factor of σ^2 . We use a Kalman filtering approach to estimate $u_{\text{post}}(t)$ and the unknown parameters in eq. (2). In the context of Kalman filtering, our time varying state vector is

$$\mathbf{X}(t) = [u_{\text{post}}(t), \dot{u}_{\text{post}}(t), c_0, \dots, c_7] \quad (4)$$

and eq. (2) is the observation function which maps the state vector to the GPS observations. We initiate the Kalman filter by assuming a prior estimate of $\mathbf{X}(t)$ at the first time epoch, denoted $\mathbf{X}_{1|0}$, which has a sufficiently large covariance, denoted $\Sigma_{1|0}$, to effectively make our prior uninformed. For each time epoch t_i , Bayesian linear regression is used to incorporate GPS derived estimates of displacement with our prior estimate of the state $\mathbf{X}_{i|i-1}$ to form a posterior estimate of the state $\mathbf{X}_{i|i}$, which has covariance $\Sigma_{i|i}$. We then use the posterior estimate of the state at time t_i to form a prior estimate of the state at time t_{i+1} through the transition function

$$\mathbf{X}_{i+1|i} = \mathbf{F}_{i+1} \mathbf{X}_{i|i} + \delta_{i+1}, \quad (5)$$

where

$$\mathbf{F}_{i+1} = \begin{bmatrix} 1 & (t_{i+1} - t_i) & \mathbf{0} \\ 0 & 1 & \mathbf{0} \\ \mathbf{0} & \mathbf{0} & \mathbf{I} \end{bmatrix} \quad (6)$$

and δ_{i+1} is the process noise, which has zero mean and covariance described by

$$\mathbf{Q}_{i+1} = \sigma^2 \begin{bmatrix} \frac{(t_{i+1}-t_i)^3}{3} & \frac{(t_{i+1}-t_i)^2}{2} & \mathbf{0} \\ \frac{(t_{i+1}-t_i)^2}{2} & (t_{i+1} - t_i) & \mathbf{0} \\ \mathbf{0} & \mathbf{0} & \mathbf{0} \end{bmatrix}. \quad (7)$$

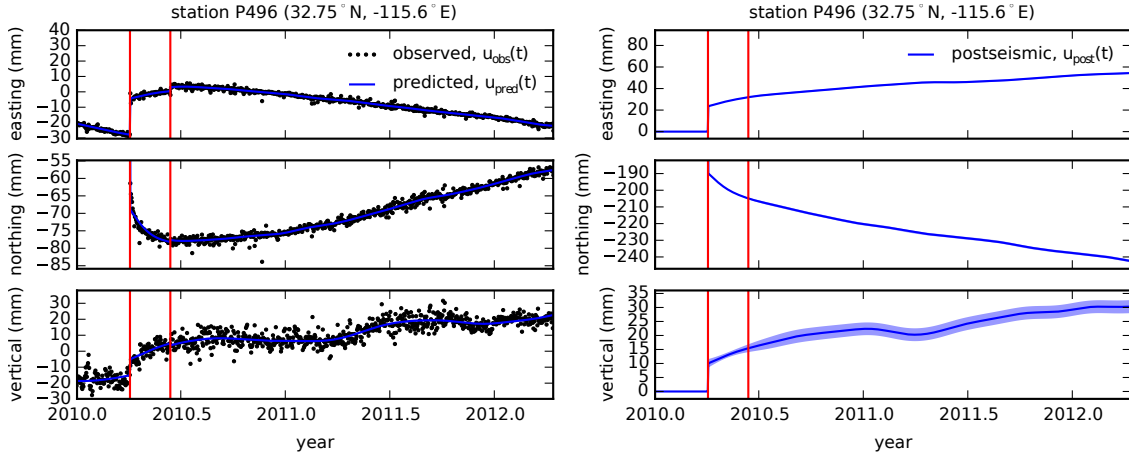


Figure 2. Left panels show GPS time series from UNAVCO (black) and the predicted displacement (blue) from eq. (2) for a near-field station. Red lines indicate the times of the El Mayor-Cucapah and Ocotillo earthquake. The right panels show estimated coseismic and postseismic displacements u_{post} which are extracted from the predicted displacements. The 68% confidence interval is shown in light blue.

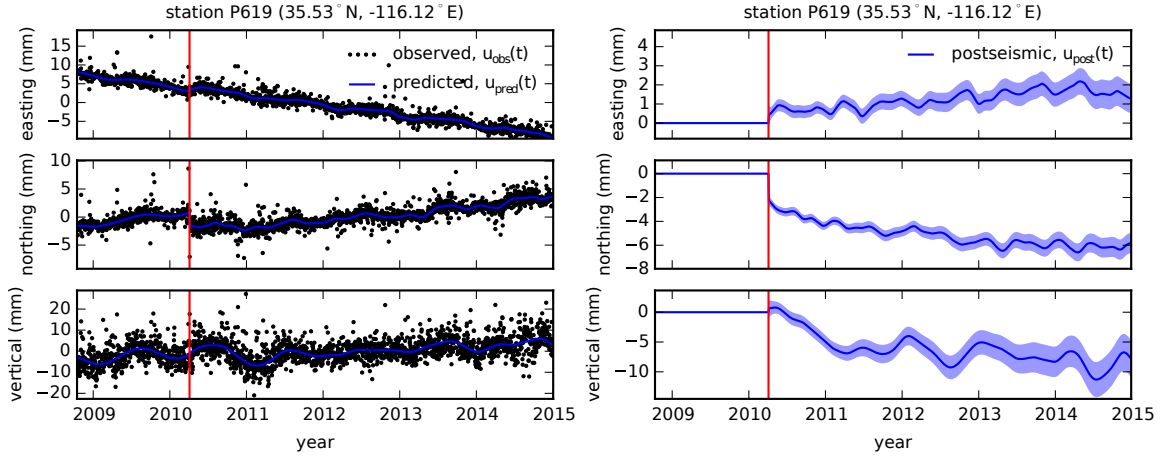
The covariance of the new prior state, $\mathbf{X}_{i+1|i}$, is then described by

$$\Sigma_{i+1|i} = \mathbf{F}_{i+1}\Sigma_{i|i}\mathbf{F}_{i+1}^T + \mathbf{Q}_{i+1}. \quad (8)$$

This process is repeated for each of the N time epochs at which point we use Rauch-Tung-Striebel smoothing [Rauch *et al.*, 1965] to find $\mathbf{X}_{i|N}$, which is an estimate of the state at time t_i that incorporates GPS observation for all N time epochs. Our final estimates of $u_{\text{post}}(t)$ are used in subsequent analysis, while the remaining components of the state vector are considered nuisance parameters. In the interests of computational tractability, we down sample our smoothed time series from daily solutions down to weekly solutions.

The smoothness of $u_{\text{post}}(t)$ is controlled by the chosen value of σ^2 , which describes how rapidly we expect postseismic displacements to vary over time. Setting σ^2 equal to zero will effectively result in modeling $u_{\text{post}}(t)$ as a straight line which is insufficient to describe the expected transient behavior in postseismic deformation. The other end member, where σ^2 is infinitely large, will result in $u_{\text{pred}}(t)$ over fitting the data. While one can use a maximum likelihood based approach for picking σ^2 [e.g. Segall and Mathews, 1997], we instead take a subjective approach and choose a value for σ^2 that is just large enough to faithfully describe the observed deformation at the most near-field station in our study, P496, which exhibits the most pronounced rapid changes in velocity. This ensures that σ^2 will be sufficiently large so that our estimate of $u_{\text{post}}(t)$ does not smooth out potentially valuable postseismic signal at the remaining stations. We find that using $\sigma^2 = 0.05\text{m}^2/\text{yr}^3$ adequately describe all but the first week of postseismic deformation at station P496, which gets incorporated into our estimate of coseismic displacements (Figure 2). We assume that the first week of deformation is overwhelmingly the result of afterslip and this afterslip is lumped into our estimates of coseismic slip. Freed *et al.* [2007] noted that postseismic deformation can be observed at distances greater than 200 km from the Hector Mine earthquake and, after filtering the time series for stations up to 400 km from the El Mayor-Cucapah epicenter, we also clearly see far reaching postseismic transient deformation (Figure 3).

It is important to note that the shown uncertainties in $u_{\text{post}}(t)$ do not account for the non-negligible epistemic uncertainty in eq. (2). For example, we assume a constant rate of secular deformation, which appears to be an appropriate approximation for all but perhaps the stations closest to the Hector Mine epicenter, as noted above. Also, our model for seasonal de-



151 **Figure 3.** same as Figure 2 but for a far-field station.

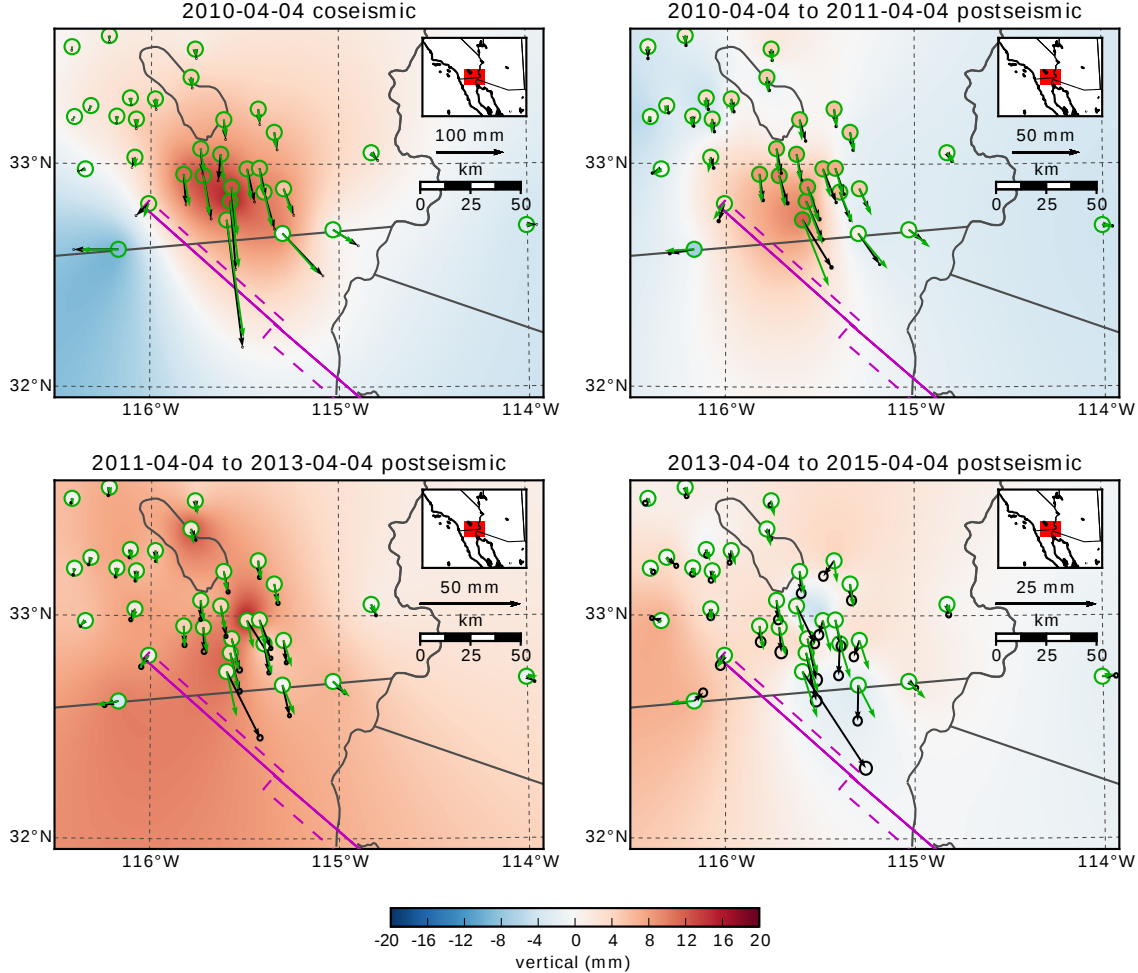
156 formation in eq. (2) assumes a constant amplitude over time, which means that any yearly vari-
 157 ability in the climatic conditions could introduce systematic residuals [Davis *et al.*, 2012]. In-
 158 deed, it would be more appropriate to consider the seasonal amplitudes $c_2 - c_5$ in eq. (2) as
 159 stochastic variables [Murray and Segall, 2005]. By using constant seasonal amplitudes, our es-
 160 timate of $u_{\text{post}}(t)$ seems to describe some of the unmodeled annual and semi-annual oscilla-
 161 tions (e.g. Figure 3).

162 We show in Figures 4 and 5 the near and far-field postseismic displacements accumu-
 163 lated over the time intervals 0-1 years, 1-3 years, and 3-5 years, as well as the coseismic dis-
 164 placements. Stations at epicentral distances beyond ~ 200 km have an elevated rate of defor-
 165 mation for the first three years following the earthquake. This far-field deformation has a south-
 166 ward trend along the direction of the El Mayor-Cucapah P axis and a similar eastward trend
 167 can be seen in the few far-field stations in Arizona, located along the T axis. After three years,
 168 the trend in far-field postseismic deformation is barely perceptible. Most far-field stations dis-
 169 play an initial subsidence for the first year after the El Mayor-Cucapah earthquake followed
 170 by continued uplift. This trend in vertical deformation can be observed in all three of the quad-
 171 rats where postseismic data is available, which means that the vertical deformation does not
 172 exhibit an anti-symmetric quadrant pattern, as would be expected for postseismic processes.
 173 Although we use vertical deformation in our analysis in Section 3, we do not put an empha-
 174 sis on trying to describe the vertical deformation as it likely does not have postseismic ori-
 175 gins.

176 The near-field postseismic deformation is notably sustained when compared to the far-
 177 field deformation. Namely, the station in this study which is closest to the El Mayor-Cucapah
 178 epicenter, P496, has been moving at a steady rate of ~ 1.5 cm/yr to the south since about one
 179 year after the El Mayor-Cucapah earthquake. Vertical postseismic deformation in the near-field
 180 does display a quadrant pattern which is consistent with the coseismic vertical deformation,
 181 suggesting that it is resulting from postseismic processes. However, the vertical postseismic
 182 signal is only apparent for the first year after the earthquake (Figure 4). As with the far-field
 183 deformation, there is a general trend of uplift in the near-field after about one year.

190 3 Postseismic Modeling

191 We seek to find the mechanisms driving five years of postseismic deformation follow-
 192 ing the El Mayor-Cucapah earthquake and we consider afterslip and viscoelastic relaxation as
 193 candidate mechanisms. Poroelastic rebound has also been used to model postseismic defor-
 194 mation [e.g. Jónsson *et al.*, 2003]; however, Gonzalez-Ortega *et al.* [2014] found that poroe-



176 **Figure 4.** Near-field coseismic and cumulative postseismic displacements over the indicated time periods
 177 (black) as well as predicted displacements for our preferred model from Section 3.3 (green). Observed vertical
 178 deformation is shown as an interpolated field and predicted vertical displacements are shown within the
 179 circles at the base of each vector. Note that the interpolant is not well constrained in Mexico where there is no
 180 data available.

| depth (km) | λ (GPa) | μ (GPa) | η_{eff} (10^{18} Pa s) | μ_k/μ |
|---------------|-----------------|-------------|---------------------------------------|-------------|
| 0-5 | 24.0 | 24.0 | - | - |
| 5-15 | 35.0 | 35.0 | - | - |
| 15-30 | 42.0 | 42.0 | 44.3 | 0.0 |
| 30-60 | 61.0 | 61.0 | 5.91 | 0.375 |
| 60-90 | 61.0 | 61.0 | 1.99 | 0.375 |
| 90-120 | 61.0 | 61.0 | 1.31 | 0.375 |
| 120-150 | 61.0 | 61.0 | 1.10 | 0.375 |
| 150- ∞ | 61.0 | 61.0 | 1.07 | 0.375 |

191 **Table 1.** Assumed and estimated material properties. λ and μ are assumed known *a priori* and are based
 192 on the values used for the coseismic model by Wei *et al.* [2011b]. The values for η_{eff} are estimated in Section
 193 3.2, and $\frac{\mu_k}{\mu}$ are the optimal shear moduli ratios found in Section 3.3 for a Zener rheology upper mantle.

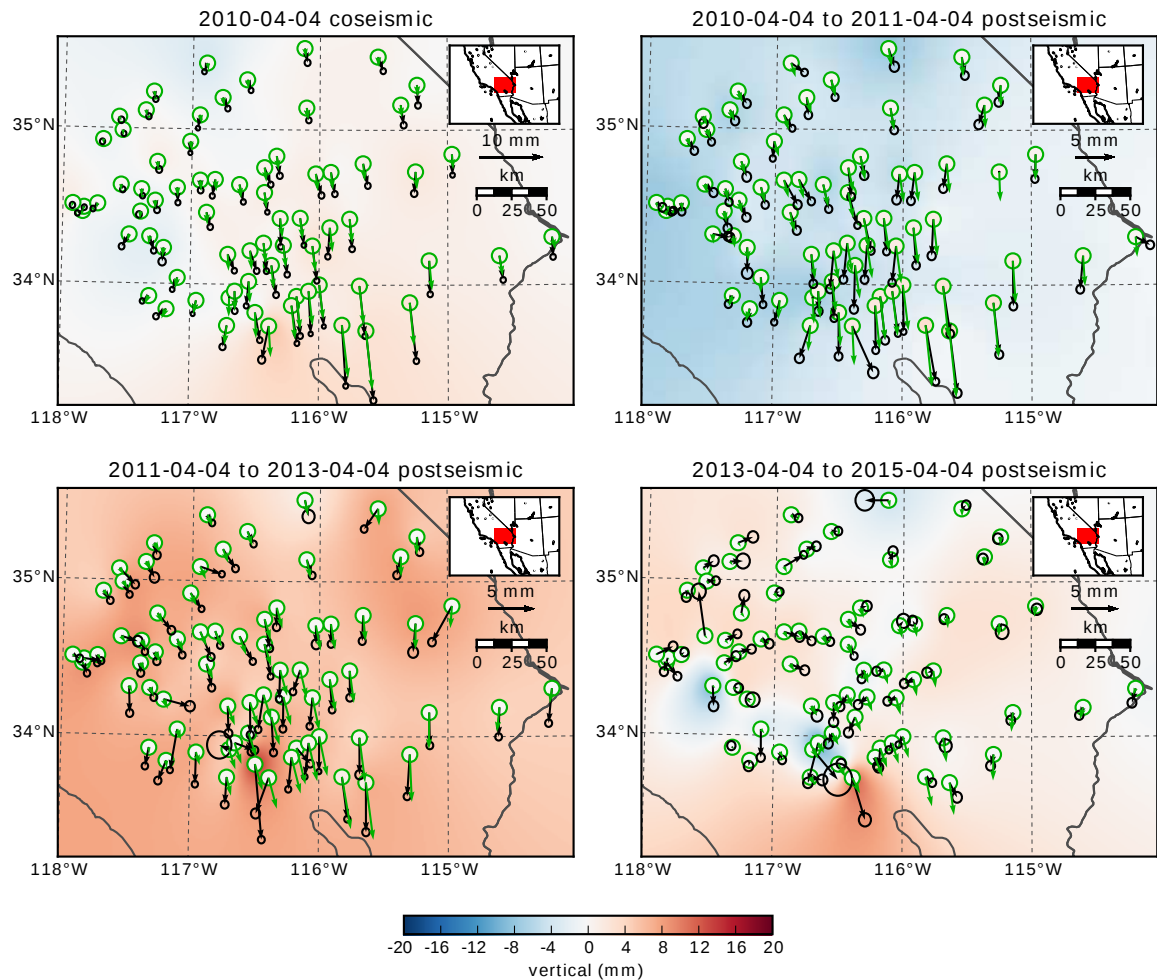


Figure 5. Same as Figure 4 but for far-field stations.

181

lastic rebound is unlikely to be a significant contributor to postseismic deformation following the El Mayor-Cucapah earthquake. Furthermore, we consider stations which are sufficiently far away from the main rupture that poroelastic rebound should be insignificant.

We estimate coseismic and time-dependent postseismic fault slip, both of which are assumed to occur on a fault geometry modified from *Wei et al.* [2011b]. Field studies [*Fletcher et al.*, 2014] and LIDAR observations [*Oskin et al.*, 2012] have revealed a significantly more complicated fault geometry than what was inferred by *Wei et al.* [2011b], especially within the Sierra Cucapah. However, we find that a relatively simple coseismic fault geometry based on [*Wei et al.*, 2011b] is adequate because most of the stations used in this study are sufficiently far from the El Mayor-Cucapah rupture zone that they are insensitive to the details in the fault geometry found by *Fletcher et al.* [2014] and *Oskin et al.* [2012]. The fault geometry used in this study (Figure 1) consists of the two main fault segments inferred by *Wei et al.* [2011b], where the northern segment runs through the Sierra Cucapah up to the US-Mexico border and the southern segment is the Indiviso fault which extends down to the Gulf of California. Both segments extend from the surface to 15 km depth. We extend the northern segment by 40 km to the north-west, motivated by the clustering of aftershocks on the northern tip of the coseismic rupture zone [*Hauksson et al.*, 2011; *Kroll et al.*, 2013]. This extended fault segment was also found to be necessary by *Rollins et al.* [2015] and *Pollitz et al.* [2012] in order to describe the postseismic deformation.

3.1 Elastic Postseismic Inversion

We consider a variety of rheologic models for the lower crust and upper mantle. The simplest rheologic model is to consider them to be effectively elastic and isotropic. In such case, the rheologic parameters consist of the Lamé parameters, λ and μ , which are reasonably well known and we use the same values used by *Wei et al.* [2011b] throughout this paper (Table 3). The only unknown is the distribution of fault slip, which can be easily estimated from postseismic deformation through linear least squares. Using a subset of the GPS stations considered in this study, *Rollins et al.* [2015] found that three years of postseismic deformation following the El Mayor-Cucapah earthquake can be explained with afterslip on the coseismic fault plane without requiring any viscoelastic relaxation. We also perform an elastic slip inversion, but we use GPS stations within a larger radius about the El Mayor-Cucapah epicenter (400 km instead of \sim 200 km). Our forward problem describing predicted postseismic deformation u_{pred} in terms of time dependent fault slip, s , is

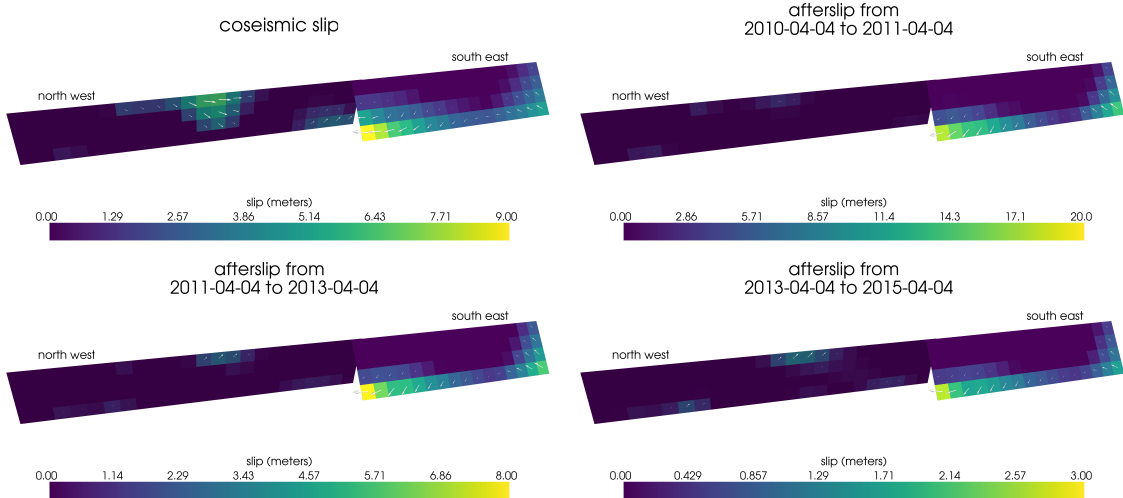
$$u_{\text{pred}}(x, t) = \int_F s(\xi, t) g(x, \xi) d\xi, \quad (9)$$

where F denotes the fault and $g(x, \xi)$ is the elastic Green's function describing displacement at surface position x resulting from slip at ξ on the fault. We estimate coseismic slip and the rate of afterslip at the discrete time intervals, 0.0-0.125, 0.125-0.25, 0.5-1.0, 1.0-2.0, 2.0-3.0, 3.0-4.0, and 4.0-5.0 years after the earthquake. Each fault segment is discretized into roughly 4 km by 4 km patches and we estimate a strike-slip and thrust component of slip for each patch. We impose that the direction of slip and slip rate are within 45° of right-lateral. We also add zeroth-order Tikhonov regularization so that our solution for s satisfies

$$\min_s \left(\left\| \frac{u_{\text{pred}}(s) - u_{\text{post}}}{\sigma_{\text{post}}} \right\|_2^2 + \lambda_s \|s\|_2^2 \right), \quad (10)$$

where σ_{post} is the uncertainty on postseismic displacements and λ_s is a penalty parameter which is chosen with a trade-off curve. We use Pylith [*Aagaard et al.*, 2013] to compute the Green's functions for this inversion as well as for the remaining inversions in this paper.

Our coseismic slip and afterslip solutions are shown in Figure 6. As with *Rollins et al.* [2015], we find that a large amount of afterslip on the southern fault segment is required to explain the observations. The potency of our inferred coseismic slip is $3.2 \times 10^9 \text{ m}^3$, equivalent to a Mw7.28 earthquake when assuming a shear modulus of 32 GPa. The potency of our



237 **Figure 6.** Coseismic slip and cumulative afterslip over the indicated intervals for the elastic model from
238 Section 3.1. Color indicates the magnitude of slip while arrows indicate the motion of the hanging wall.

225 inferred cumulative five years of afterslip is $6.1 \times 10^9 \text{ m}^3$, equivalent to a Mw7.46 earthquake,
226 which is unrealistically large if we consider afterslip to be driven by coseismically induced
227 stresses. Figure 7 shows the time series for the observed and predicted postseismic displace-
228 ments at stations along the El Mayor-Cucapah P axis. We show the radial component of dis-
229 placements with respect to the El Mayor-Cucapah epicenter and we also rescale the displace-
230 ments so that the difference between the minimum and maximum observed displacements are
231 the same for each station. Our elastic slip model accurately describes near-field postseismic
232 deformation and systematically underestimates postseismic deformation at epicentral distances
233 $\gtrsim 150 \text{ km}$. When the fault segments used in the inversion are extended down to 30 km depth,
234 rather than 15 km, the systematic far-field residuals are smaller but remain apparent. Because
235 an elastic model requires an unrealistic amount of afterslip and is unable to predict far-field
236 deformation, we move on to consider viscoelastic models in the next section.

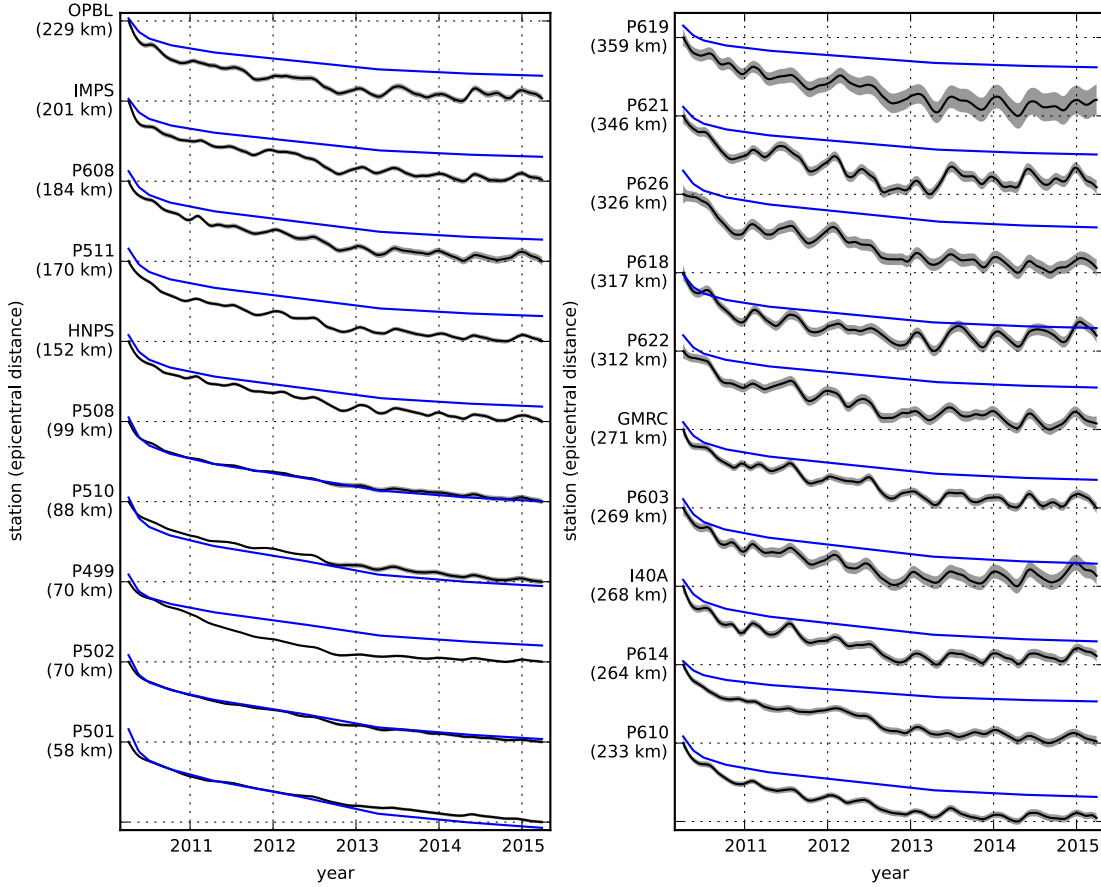
244 3.2 Early Postseismic Inversion

245 For any linear viscoelastic rheology of the crust and mantle, postseismic displacements
246 resulting from time dependent fault slip can be described as

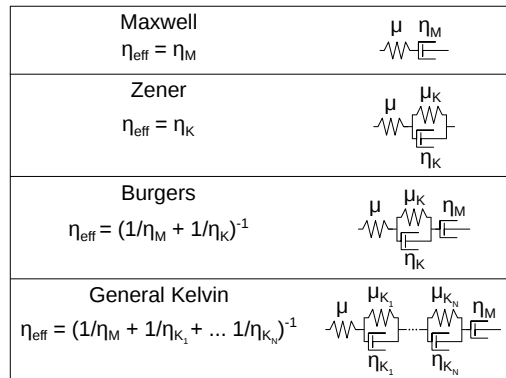
$$247 u_{\text{pred}}(x, t) = \int_F s(\xi, t) g(x, \xi) d\xi + \int_0^t \int_F s(\xi, \tau) f(t - \tau, x, \xi) d\xi d\tau, \quad (11)$$

248 where $f(t, x, \xi)$ describes the time-dependent velocity at x resulting from viscoelastic relax-
249 ation of stresses induced by slip at ξ . f is a function of λ , μ , and any additional rheologic pa-
rameters controlling the viscoelastic response, which are generally not well known. Schematic
representations of the viscoelastic rheologic models considered in this study are shown in Fig-
ure 8. We discuss these rheologic models and their use in geophysical studies in Section 4.

250 In order to greatly simplify the inverse problem, we use the method described in *Hines*
251 and *Hetland* [2016] to constrain an initial effective viscosity structure from the early postseis-
252 mic deformation. Our method utilizes the fact that coseismic stresses throughout the crust and
253 upper mantle depend on the instantaneous elastic parameters and are independent of the vis-
254 coelastic parameters which we wish to estimate. Immediately following an earthquake, each
255 parcel will have a strain rate that is proportional to the coseismic stress and inversely propor-
256 tional to the parcel's effective viscosity, η_{eff} . Using one-dimensional viscoelastic models, we



239 **Figure 7.** Scaled radial component of observed postseismic displacements u_{obs} (black) and displacements
 240 predicted by the best fitting elastic model u_{pred} (blue). Downward motion indicates that the station is moving
 241 toward the El Mayor-Cucapah epicenter. Displacement time series are scaled so that the minimum and maximum
 242 observed values lie on the grid lines. The 68% confidence interval for the observed displacements are
 243 shown in gray.



250 **Figure 8.** Schematic illustration of the rheologic models considered in this paper as well as their effective
 251 viscosities.

define the effective viscosity as

$$\eta_{\text{eff}} = \frac{\sigma}{\dot{\varepsilon}} \Big|_{t=0}, \quad (12)$$

where σ is an applied stress at $t = 0$ and $\dot{\varepsilon}$ is the resulting strain rate. Figure 8 shows how η_{eff} relates to the parameters for various linear viscoelastic rheologies. We can deduce that the initial rate of surface deformation resulting from viscoelastic relaxation is a summation of the surface deformation resulting from relaxation in each parcel, scaled by the reciprocal of the parcel's effective viscosity. That is to say

$$f(0, x, \xi) = \int_L \frac{h(x, \xi, \zeta)}{\eta_{\text{eff}}(\zeta)} d\zeta, \quad (13)$$

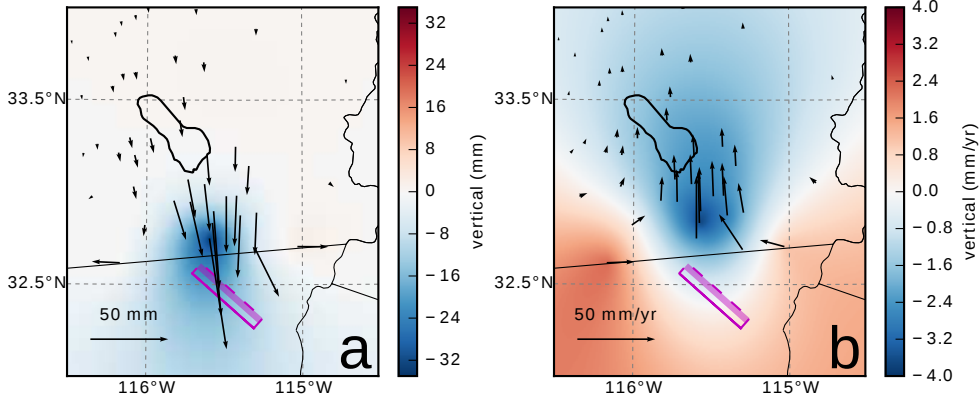
where L denotes the crust and mantle and $h(x, \xi, \zeta)$ describes the initial rate of deformation resulting from viscoelastic relaxation at ζ induced by slip at ξ . We can combine eq. (13) with eq. (11) to get a first order approximation for early postseismic deformation,

$$u_{\text{pred}}(x, t) \approx \int_F s(\xi, t) g(x, \xi) d\xi + \int_0^t \int_F \int_L \frac{s(\tau, \xi)}{\eta_{\text{eff}}(\zeta)} h(x, \xi, \zeta) d\zeta d\xi d\tau, \quad (14)$$

which is valid for as long as the rate of deformation resulting from viscoelastic relaxation is approximately constant. Although eq. (14) may only be valid for a short portion of the post-seismic period, its utility becomes apparent when noting that g and h are only functions of the fault geometry and instantaneous elastic properties, λ and μ , and thus g and h can be computed numerically as a preprocessing step. The forward problem in eq. (14) can then be rapidly evaluated for any realization of s and η_{eff} . This is in contrast to evaluating the full forward problem, eq. (11), numerically for each realization of s and the unknown rheologic properties.

Details on how eq. (14) is used to estimate s and η_{eff} from postseismic deformation can be found in *Hines and Hetland* [2016]. A non-linear Kalman filter based inverse method can also be used to estimate s and η_{eff} in a manner akin to *Segall and Mathews* [1997] or *McGuire and Segall* [2003], in which we would not have to explicitly impose a time dependent parametrization of s . We have thoroughly explored Kalman filter based approaches, but we ultimately prefer the method described in *Hines and Hetland* [2016] because of its relative simplicity. Moreover, we believe the piecewise continuous representation of slip with respect to time to be sufficiently general for the resolving power of these GPS data.

We estimate coseismic slip and afterslip with the same spatial and temporal discretization as in Section 3.1. Simultaneously, we estimate η_{eff} within six vertically stratified layers which have depths ranging from 15-30 km, 30-60 km, 60-90 km, 90-120 km, 120-150 km, as well as from 150 km to the bottom of our numerical model domain at 800 km. We again restrict fault slip to occur between 0 and 15 km depth, which is done in order to help eliminate inevitable non-uniqueness in the inversion. It has long been recognized that fault slip at sufficiently great depths can produce surface deformation that is indistinguishable from viscoelastic relaxation, at least in two-dimensional earthquake models [Savage, 1990]. Additionally, we note that when simultaneously estimating both afterslip and viscosity in the lower crust, the inverse problem becomes particularly ill-posed. This ill-posedness is illustrated in Figure 9, which shows the displacements resulting from a meter of slip on a fault extending from 15 to 30 km depth and the initial velocity resulting from subsequent viscoelastic relaxation in the lower crust, which is given a viscosity of 10^{18} Pa s. In this demonstration, the viscoelastic relaxation is entirely driven by the fault slip in the lower crust. The horizontal displacements from fault slip are in the opposite direction as the displacements resulting from viscoelastic relaxation. This means that surface displacements resulting from afterslip at lower crustal depths can be cancelled out, at least partially, by a low viscosity lower crust. We eliminate this null space by allowing only one mechanism in the lower crust, which we choose to be viscoelastic relaxation. This is not to say that we do not believe deep afterslip to be a possibility; rather, we restrict slip to seismogenic depths as a modeling necessity. Although, it has been noted that the pattern of vertical postseismic deformation following the El Mayor-Cucphuong earthquake indicates that a significant amount of afterslip must be shallow [Rollins *et al.*, 2015].



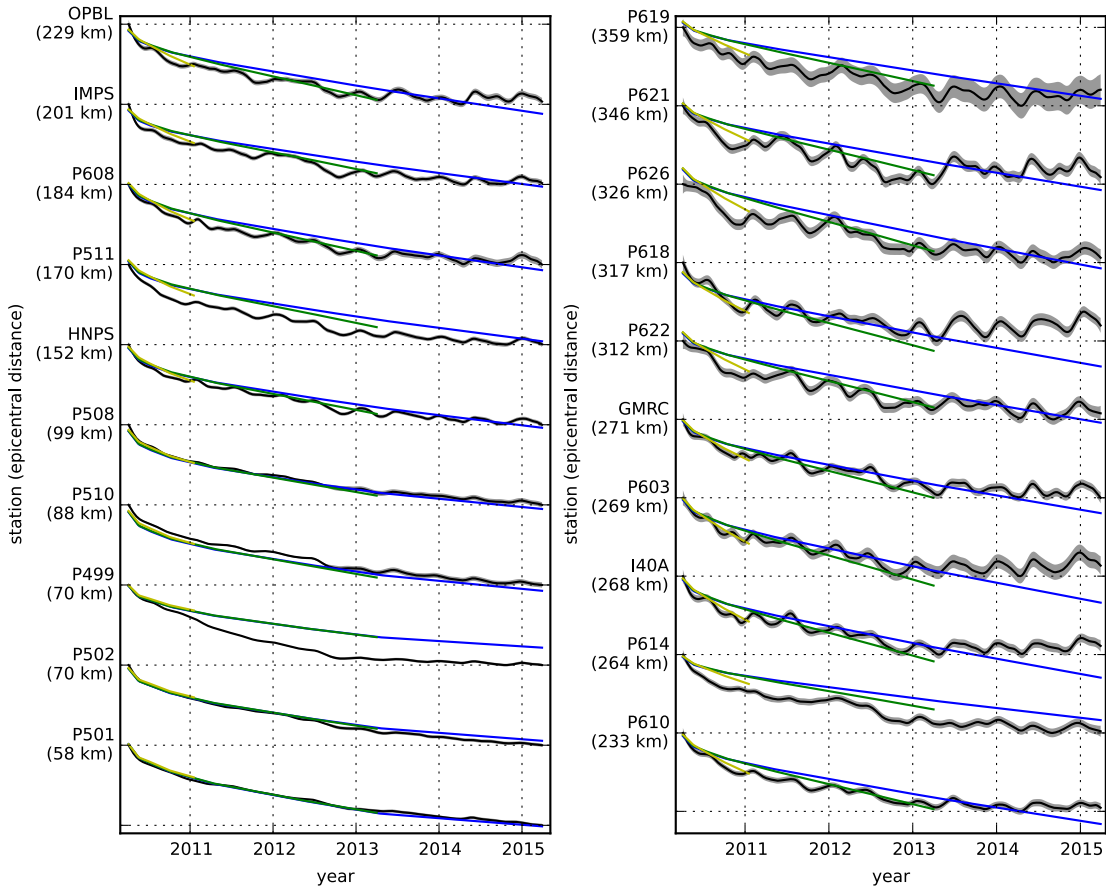
290 **Figure 9.** Displacements resulting from fault slip at lower crustal depths (a), and initial velocities resulting
 291 from subsequent relaxation of a viscoelastic lower crust (b). The fault segment dips 75° to the north-east and
 292 its surface projection is outlined in magenta. The highlighted area on the fault extends from 15 to 30 km depth
 293 and indicates where 1 meter of right-lateral slip was imposed. The elastic properties of the crust and mantle
 294 are the same as in Table 3, and η_{eff} is 10^{18} Pa s in the lower crust. Vertical displacements are interpolated
 295 between station locations.

296 We must determine at which point the early postseismic approximation breaks down, which
 297 we will denote as t_{bd} . As noted, eq. (14) is valid for approximately as long as the rate of de-
 298 formation resulting from viscoelastic relaxation is approximately constant. We can almost cer-
 299 tainly assume that deformation at the most far-field stations, which are ~ 400 km away from
 300 the El Mayor-Cucapah epicenter, is the result of viscoelastic relaxation. The approxima-
 301 tion should then be valid for as long as a linear trend adequately approximates the far-field de-
 302 formation. Using this logic, it would appear that t_{bd} is about one year after the El Mayor-Cucapah
 303 earthquake. Another way to determine t_{bd} is to find the best fitting prediction of eq. (14) to
 304 observed deformation using increasing durations of the postseismic time series. t_{bd} should be
 305 the point when eq. (14) is no longer capable of describing the observed deformation without
 306 incurring systematic misfits. When using eq. (14) to fit the entire five years of postseismic dis-
 307 placements, we see that the near-field displacements (e.g., station P501) are accurately pre-
 308 dicted. When looking at displacements in the far-field (e.g., station P621), we see that eq. (14)
 309 overestimates the rate of deformation in the later postseismic period and underestimates the
 310 rate of deformation in the early period (Figure 10). Due to the low signal-to-noise ratios for
 311 far-field stations, it is difficult to determine at what point eq. (14) is no longer able to predict
 312 the observed displacements; however, we settle on $t_{\text{bd}} = 0.8$ years after the earthquake, while
 313 acknowledging that the choice is subjective. As noted in Hines and Hetland [2016], overes-
 314 timating t_{bd} will result in a bias towards overestimating η_{eff} , while picking a t_{bd} which is too
 315 low will not necessarily result in a biased estimate of η_{eff} , although the uncertainties would
 316 be larger. We can then consider inferences of η_{eff} to be an upper bound on the viscosity needed
 317 to describe the far-field rate of deformation during the first 0.8 years of postseismic deforma-
 318 tion.

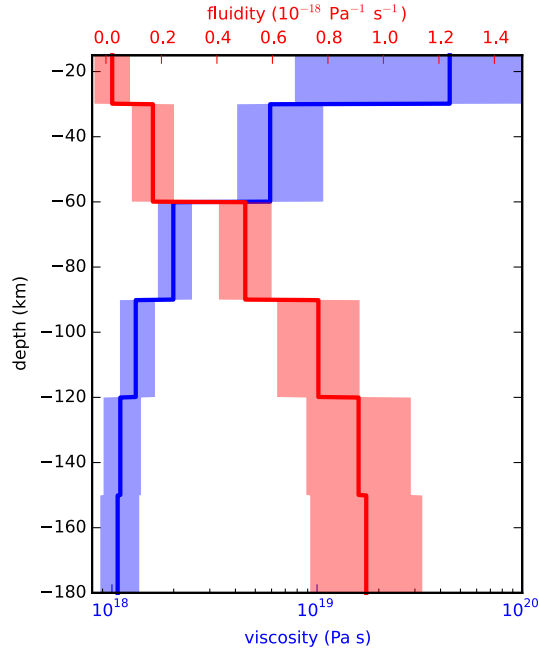
We estimate coseismic slip, afterslip, and effective viscosities by solving

$$\min_{s, \eta_{\text{eff}}} \left(\left\| \frac{u_{\text{pred}}(s, \eta_{\text{eff}}) - u_{\text{post}}}{\sigma_{\text{post}}} \right\|_2^2 + \lambda_s \|s\|_2^2 + \lambda_\eta \|\nabla \eta_{\text{eff}}^{-1}\|_2^2 \right), \quad (15)$$

321 where u_{post} consists of the first 0.8 years of postseismic deformation and u_{pred} are the pre-
 322 dicted displacements from eq. (14). Due to inherent non-uniqueness, we have added zeroth-
 323 order Tikhonov regularization to estimates of s and second-order Tikhonov regularization to
 324 estimates of effective fluidity η_{eff}^{-1} . The degree to which we impose the regularization on slip



319 **Figure 10.** Observed postseismic displacements (black) and best fitting predictions of eq. (14) to 5.0 (blue),
 320 3.0 (green), and 0.8 (yellow) years of the postseismic data.

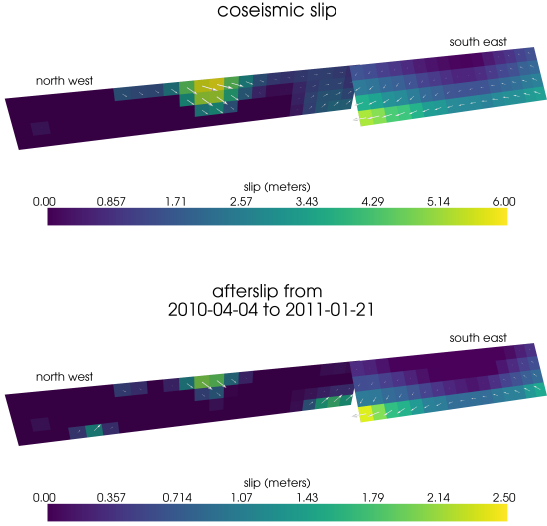


345 **Figure 11.** Effective viscosities and associated fluidities inferred by fitting eq. (14) to the first 0.8 years of
 346 postseismic displacements. 95% confidence intervals, estimated from bootstrapping, are indicated by color
 347 fields.

325 and fluidity is controlled by the penalty parameters λ_s and λ_η , which are chosen with trade-
 326 off curves. Our goal here is to get a prior constraint on η_{eff} to minimize the amount of search-
 327 ing we have to do when describing the postseismic deformation over the full five years, which
 328 we do in Section 3.3. Estimates of s made here will not be used in Section 3.3, and so the
 329 motivation behind adding regularization to s is to ensure that the slip driving viscoelastic re-
 330 laxation in eq. (14) is sensible.

331 Our estimated effective viscosities, and corresponding fluidities, are shown in Figure 11.
 332 Although fluidity is rarely used in geophysical literature, eq. (13) is linear with respect to flu-
 333 idity and so the fluidity indicates the amplitude of the viscoelastic signal coming from each
 334 layer. We also show the 95% confidence intervals for estimated viscosities and fluidities but
 335 we note that the uncertainties tend to be underestimated due to the added regularization [Aster
 336 *et al.*, 2011]. A robust feature that we see is that the largest jump in fluidity is at 60 km depth,
 337 which is consistent with the range of lithosphere-asthenosphere boundary depths inferred by
 338 Lekic *et al.* [2011]. This transitional depth is also consistent with the the viscosity structure
 339 required to explain far-field postseismic deformation following the Hector Mine earthquake
 340 [Freed *et al.*, 2007]. We find that the viscosity below 60 km depth needs to be $\sim 10^{18}$ Pa s to
 341 describe the early rate of postseismic deformation at far-field stations while the lower crust
 342 and uppermost mantle need to be relatively stronger. The viscosity of the lower crust is the
 343 least well constrained as there is no evidence of relaxation in that layer, meaning that it is ef-
 344 fectively elastic over the first 0.8 years after the earthquake.

348 Our initial estimate for coseismic slip and cumulative afterslip over the first 0.8 years
 349 after the El Mayor-Cucapah earthquake are shown in Figure 12. Similar to our elastic slip model
 350 from Section 3.1, a significant amount of right-lateral and normal coseismic slip is inferred
 351 to be on the Sierra Cucapah fault segment. Our coseismic slip solution is consistent with field
 352 studies [Fletcher *et al.*, 2014] and the model from Wei *et al.* [2011b]. The potency of inferred
 353 coseismic slip is 3.3×10^9 m³, which is also about the same as that inferred from Section
 354 3.1. The present inference of afterslip on the Indiviso fault is significantly less than what was



363 **Figure 12.** Coseismic slip and afterslip inferred by fitting eq. (14) to the first 0.8 years of postseismic
364 displacements.

355 found in the Section 3.1 where we did not account for viscoelasticity. When fault slip is si-
356 multaneously estimated with viscosity, the potency of inferred afterslip over the first 0.8 years
357 after the earthquake is $0.85 \times 10^9 \text{ m}^3$, compared to $3.5 \times 10^9 \text{ m}^3$ when we assume the crust
358 and upper mantle are elastic. The significant amount of afterslip inferred on the Indiviso fault
359 seems to be compensating for unmodeled viscoelastic relaxation at depths greater than 60 km.
360 The fact that there is still an appreciable amount of afterslip inferred on the Indiviso fault raises
361 the question of whether it is compensating for viscoelastic relaxation that is more localized
362 than what we allow for since we only estimate depth dependent variations in viscosity.

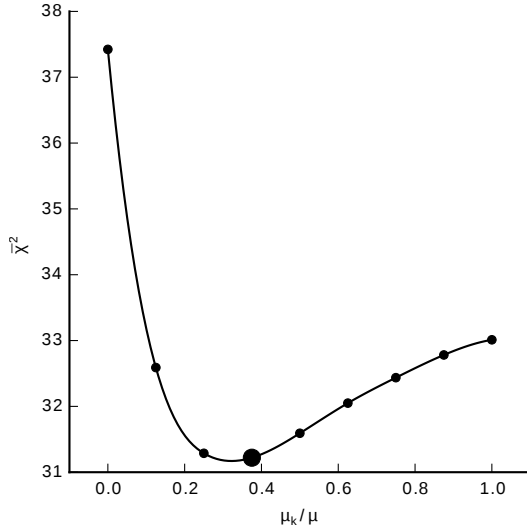
365 3.3 Full Postseismic Inversion

In the previous section, we used the inverse method from *Hines and Hetland* [2016] to constrain the effective viscosity structure required to explain the first 0.8 years of postseismic deformation. In this section, we use these effective viscosities as a prior constraint when searching for models which are capable of describing the available five years of postseismic data, where our forward problem is now eq. (11) rather than the approximation given by eq. (14). We perform a series of fault slip inversions assuming a variety of rheologies for the lower crust and upper mantle which are consistent with our findings from Section 3.2. We appraise each model using the mean chi-squared value,

$$\bar{\chi}^2 = \frac{1}{N} \left\| \frac{u_{\text{pred}} - u_{\text{obs}}}{\sigma_{\text{obs}}} \right\|_2^2, \quad (16)$$

366 where N is the number of observations.

We first assume that the crust and mantle can be described with a Maxwell rheology, and we set the steady-state viscosity η_M equal to our inference of η_{eff} . We compute f and g from eq. (11) using Pylith, and we use the same spatial and temporal discretization of s as in Sections 3.1 and 3.2. We estimate s using linear least squares and find a misfit of $\bar{\chi}^2 = 37.4$. For comparison, $\bar{\chi}^2 = 35.3$ for the elastic model from Section 3.1. The Maxwell viscoelastic model has a larger misfit because it tends to overestimate the rate of deformation after about three years (Figure 14). Since our initial estimates of η_{eff} may be biased towards overestimating viscosities, we have also performed the slip inversion where we use uniformly lower



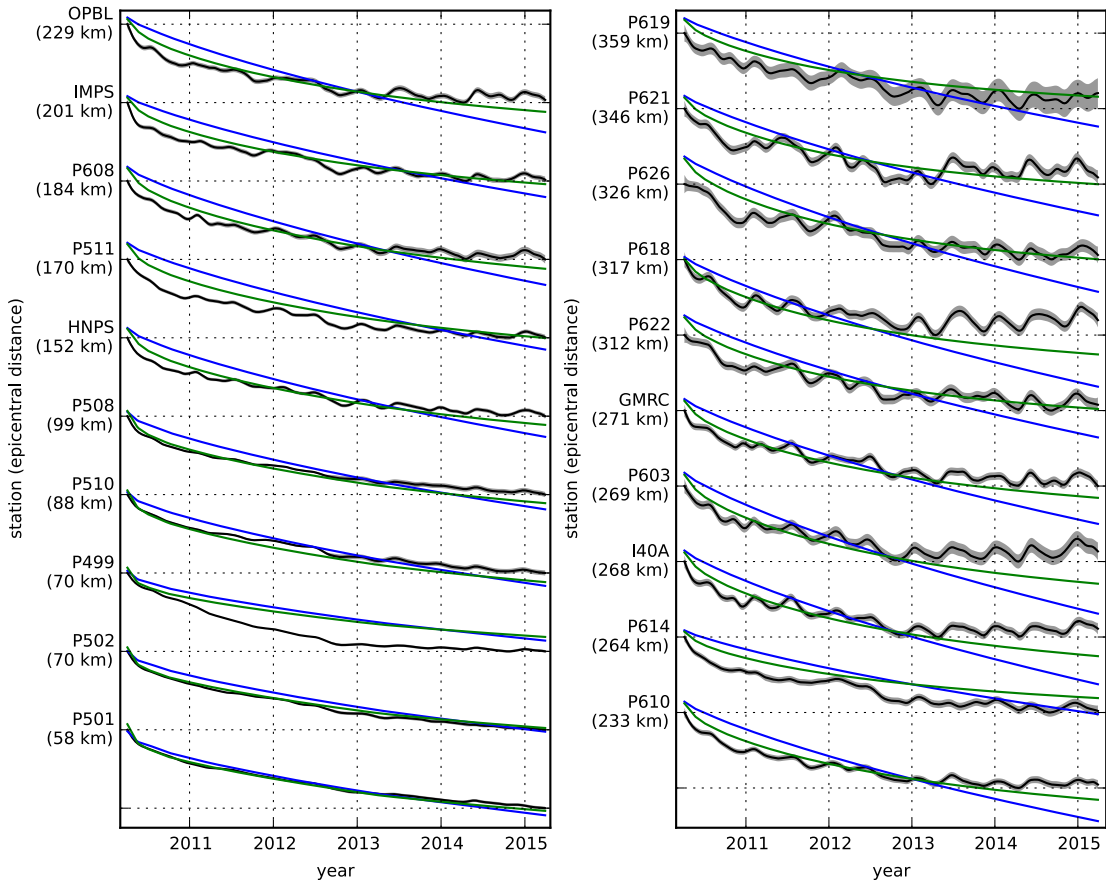
396 **Figure 13.** Mean chi-squared value for the best fitting slip model as a function of the transient shear modu-
 397 lus relative to the elastic shear modulus in a Zener upper mantle. Large dot indicates our preferred ratio.

375 viscosities in the crust and mantle. However, decreasing the viscosity only increases the mis-
 376 fit. Although, the viscosities used here are consistent with the successful Maxwell viscoelas-
 377 tic models found by *Rollins et al.* [2015] and *Spinler et al.* [2015], which had mantle viscosities
 378 on the order of 10^{18} Pa s and relatively higher lower crustal viscosities, we find that such
 379 a model is incapable of describing the entire postseismic time series. *Pollitz et al.* [2001] simi-
 380 larly recognized this deficiency in a Maxwell rheology, which then motivated their exploration
 381 of a Burgers rheology upper mantle [*Pollitz*, 2003].

382 Instead of exploring a Burgers rheology mantle, which introduces two new parameters
 383 that need to be estimated, the transient viscosity η_K and transient shear modulus μ_K , we first
 384 consider a Zener rheology for the mantle, which only introduces one additional unknown pa-
 385 rameter, μ_K . We assume that the lower crust still has a Maxwell rheology. The steady-state
 386 viscosity in the crust and the transient viscosity in the mantle are set equal to the inferred ef-
 387 fective viscosities. We then estimate the ratio of shear moduli $\frac{\mu_K}{\mu}$. We compute nine differ-
 388 ent sets of Green's functions, f and g , where we assume values of $\frac{\mu_K}{\mu}$ ranging from 0 to 1.
 389 The former being a degenerate case where the Zener model reduces to the above Maxwell model.
 390 We estimate coseismic slip and afterslip for each realization of $\frac{\mu_K}{\mu}$. The shear moduli ratio
 391 that yields the best prediction to the observed postseismic displacements is found to be 0.375
 392 which produces a misfit of $\bar{\chi}^2 = 31.2$ (Figure 13). The improvement in the Zener model over
 393 the Maxwell model can be clearly seen in the fit to the far-field data (Figure 14). The Zener
 394 model does a significantly better job at explaining the transient rate of far-field deformation
 395 throughout the five years.

403 Because we are able to adequately describe the available five years of postseismic de-
 404 formation with a Zener model, we do not find it necessary to explore the parameter space for
 405 a more complicated Burgers rheology. However, since the Zener model is a Burgers model with
 406 an infinite steady-state viscosity, we can conclude that any Burgers rheology that has a trans-
 407 sient viscosity consistent with that found in Section 3.2 and a steady-state viscosity $\gtrsim 10^{20}$
 408 Pa s, which is effectively infinite on the time scale of five years, would also be able to sat-
 409 isfactorily describe the observable postseismic deformation.

410 The regularized inference of coseismic slip and afterslip for our preferred Zener model
 411 is shown in Figure 15. The inferred coseismic potency is 3.0×10^9 m³, equivalent to a Mw7.26
 412 earthquake, and most of the slip is shallow and on the Sierra Cucapah fault segment. The po-



398 **Figure 14.** Observed postseismic displacements (black). Predicted postseismic displacements for the best
 399 fitting slip model when assuming a Maxwell viscoelastic lower crust and upper mantle (blue). Predicted post-
 400 seismic displacements for the best fitting slip model when assuming a Maxwell viscoelastic lower crust and a
 401 Zener viscoelastic upper mantle (green). The effective viscosities are the same for both models and are shown
 402 in Figure 11.

tency of five years of afterslip is 1.1×10^9 m³. Most of the afterslip in our preferred model occurs within the first year after the earthquake and coincides with the location of our inferred coseismic slip. Inferred afterslip within the first year is accounting for the most rapid near-field transient deformation. After one year, afterslip is inferred to be deeper down on the Sierra Cucapah segment, which is describing much of the sustained near-field postseismic deformation. We emphasize, that the GPS station closest to where we infer afterslip, P496, is still about 30 km away, which is too far for us to conclusively argue for sustained localized deformation rather than shallow distributed deformation. The deep afterslip inferred after one year could potentially be describing deformation resulting from lower crustal flow. To test this, we have modified our preferred model by decreasing the lower crustal viscosity from 5.91×10^{19} Pa s to 1×10^{19} Pa s, which is still consistent with our viscosity inference from Section 3.2, and inverted for fault slip. We find that a model with a weaker lower crust adequately describes the postseismic displacements without any afterslip after one year, while still requiring about the same amount of afterslip over the first year. We do believe that the early shallow afterslip on the Sierra Cucapah segment is a robust feature in our preferred model, while we are not confident in our inference of later deep afterslip.

the postseismic displacements predicted by our preferred model are shown in Figures 4, 5 and 14. Overall, the trends in the near-field and far-field transient deformation are accurately described. In particular, the trends in far-field deformation are much better described by our preferred Zener model than either an elastic model or a model with a Maxwell viscoelastic mantle (Figure 14). There are a few areas where we have notable misfit. Most of our misfit is for the near-field stations in the Imperial Valley, and we attribute this misfit to our relatively simple fault geometry, which does not account for potential fault slip in the Imperial Valley triggered by the El Mayor-Cucapah earthquake [Wei *et al.*, 2011a, 2015]. In particular, we are unable to model the sustained, rapid rate of deformation at station P496, which suggests that this station could be influenced by a more localized deformation mechanism than is considered in this study. Additionally, we see systematic misfit in the later postseismic period west of the Landers and Hector Mine earthquakes, which may be the result of unmodeled postseismic deformation resulting from those earthquakes. Lastly, there are clear discrepancies between the observed and predicted vertical deformation following the first year after the El Mayor Cucapah earthquake. We observe a broad uplift throughout Southern California, which is inconsistent with any postseismic model.

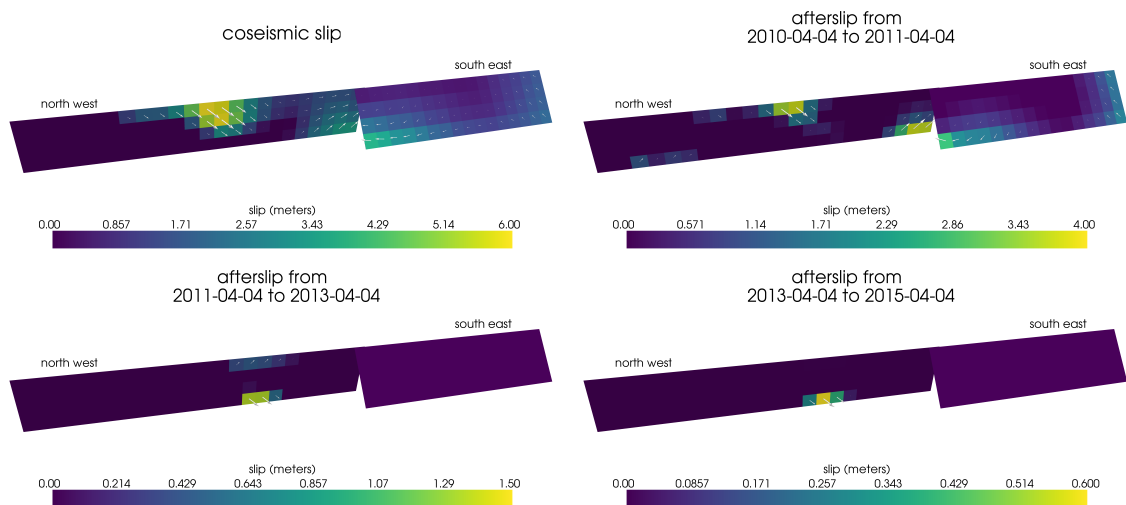


Figure 15. Inferred coseismic slip and afterslip when assuming a Maxwell rheology in the lower crust and a Zener rheology in the upper mantle. The transient viscosity η_K in the mantle and steady-state viscosity η_M in the crust are set equal to the effective viscosities from Figure 11. We set $\frac{\mu_K}{\mu} = 0.375$ in the upper mantle.

448 **4 Discussion**

449 It has long been recognized that deep afterslip and viscoelastic relaxation following an
 450 upper crustal earthquake can result in similar horizontal ground deformation at the surface [e.g.
 451 *Savage*, 1990; *Pollitz et al.*, 2001; *Hearn*, 2003; *Feigl and Thatcher*, 2006]. The similarity of
 452 the horizontal postseismic deformation results in a non-uniqueness in inferences of afterslip
 453 or viscoelastic relaxation. In contrast, the spatial pattern of vertical postseismic deformation
 454 has been proposed to be a discriminant between deep afterslip and viscoelastic relaxation [e.g.
 455 *Pollitz et al.*, 2001; *Hearn*, 2003]. It is, however, important to note that patterns of vertical de-
 456 formation are very sensitive to the depth-dependence of viscosity below the upper crust [*Yang*
 457 and *Toksöz*, 1981; *Hetland and Zhang*, 2014]. The similarity between deformation resulting
 458 from deep afterslip and viscoelastic relaxation of coseismic stresses is different from the ill-
 459 posedness described in Section 3.2. In our method, any inferred afterslip will also mechani-
 460 cally drive additional viscoelastic relaxation. The horizontal deformation resulting from deep
 461 afterslip will generally be in the opposite direction as horizontal deformation resulting from
 462 viscoelastic relaxation of subsequent stresses in the lower crust (Figure 9). As a result, there
 463 is a trade-off between inferences of deep afterslip and lower crustal viscosity. In our synthetic
 464 tests in *Hines and Hetland* [2016], we have found that inverting surface deformation for af-
 465 terslip and viscosity within the same depth interval tends to result in overestimated afterslip
 466 and an underestimated viscosity.

467 Most postseismic studies assume Maxwell viscoelasticity in the lower crust and upper
 468 mantle [e.g. *Nur and Mavko*, 1974; *Pollitz et al.*, 2000; *Hetland*, 2003; *Freed et al.*, 2006; *John-*
 469 *son et al.*, 2009; *Hearn et al.*, 2009], which is the simplest viscoelastic rheologic model. In South-
 470 ern California, postseismic studies following the Landers [*Pollitz et al.*, 2000], Hector Mine
 471 [*Pollitz et al.*, 2001], and El Mayor-Cucapah earthquake [*Spinler et al.*, 2015; *Rollins et al.*, 2015],
 472 have assumed Maxwell viscoelasticity in the lower crust and upper mantle and have inferred
 473 upper mantle viscosities on the order of 10^{17} to 10^{18} Pa s and lower crust viscosities $\gtrsim 10^{19}$
 474 Pa s. These postseismic studies are consistent with *Kaufmann and Amelung* [2000] and *Cava-*
 475 *alié et al.* [2007], who found that an upper mantle viscosity of 10^{18} Pa s and a crustal viscos-
 476 ity $\gtrsim 10^{20}$ Pa s are necessary to describe subsidence resulting from changes in loading from
 477 Lake Mead. This isostatic adjustment is a process with similar spatial and temporal scales as
 478 postseismic deformation, and thus the inferred viscosities of these two types of studies would
 479 likely agree. While these studies found viscosities that are consistent with our effective vis-
 480 cosities from Section 3.2, they are inconsistent with viscosity estimates made from geophys-
 481 ical processes that occur over longer time scales. For example, *Lundgren et al.* [2009] found
 482 that lower crust and upper mantle viscosities on the order of 10^{21} and 10^{19} Pa s, respectively,
 483 are needed to describe interseismic deformation along the Southern San Andreas fault zone
 484 in the Salton Sea region. An even higher mantle viscosity, on the order of 10^{20} Pa s, is re-
 485 quired to describe isostatic adjustment resulting from the draining of Lake Bonneville, which
 486 occurs on the time scales of 10^4 years [*Crittenden*, 1967; *Bills and May*, 1987].

487 An additional deficiency with the Maxwell rheology is that it predicts a steady decay
 488 in the rate of postseismic deformation over time, which fails to describe the commonly ob-
 489 served rapid, early transience followed by a relatively steady rate of postseismic deformation.
 490 One could explain the early transient postseismic deformation with fault creep and the later
 491 phase with relaxation in a Maxwell viscoelastic lower crust and upper mantle [e.g. *Hearn et al.*,
 492 2009; *Johnson et al.*, 2009]. However, postseismic deformation at distances greater than ~ 200
 493 km from the El Mayor-Cucapah epicenter can only be attributed to viscoelastic relaxation [*Freed*
 494 *et al.*, 2007] and we have demonstrated that the far-field deformation cannot be explained with
 495 a Maxwell rheology (Figure 14).

496 We found that a Zener rheology in the upper mantle with a transient viscosity of $\sim 10^{18}$
 497 Pa s does a noticeably better job at predicting far-field postseismic deformation. A general-
 498 ization of the Zener viscoelastic model, schematically represented as several Kelvin elements
 499 connected in series, is commonly used to describe seismic attenuation [*Liu et al.*, 1976]. The
 500 highest viscosity needed to describe seismic attenuation is on the order of 10^{16} Pa s [*Yuen and*

501 *Peltier*, 1982] which has a characteristic relaxation time on the order of days. Even though
 502 our inferred transient viscosity is orders of magnitude larger than that required for seismic at-
 503 tenuation models, the two models are not incompatible. Rather, the delayed elasticity in seis-
 504 mic attenuation models occurs on such short time scales that it can be considered part of the
 505 instantaneous elastic phase of deformation associated with the preferred Zener model in this
 506 study.

507 Of course, it has long been recognized that a Zener rheology provides an incomplete de-
 508 scriptions of the asthenosphere, as it does not have the fluid-like behavior required to explain
 509 isostatic rebound or convection in the mantle [*O'Connell*, 1971]. *Yuen and Peltier* [1982] pro-
 510 posed a Burgers rheology with a low transient viscosity ($\eta_K \approx 10^{16}$ Pa s) and high steady-
 511 state viscosity ($\eta_M \approx 10^{21}$ Pa s) to describe both seismic attenuation and long term geologic
 512 processes. The justification of a Burger's rheology mantle is further supported by laboratory
 513 experiments on olivine [*Chopra*, 1997]. *Pollitz* [2003] sought to describe postseismic defor-
 514 mation following Hector Mine with a Burgers rheology mantle and they found a best fitting
 515 transient viscosity of 1.6×10^{17} Pa s and steady-state viscosity of 4.6×10^{18} Pa s. While
 516 the Burgers rheology was introduced as a means of bridging the gap between relaxation ob-
 517 served in long and short term geophysical processes, the inferred steady state viscosity from
 518 *Pollitz* [2003] is still inconsistent with the Maxwell viscosities inferred from studies on the earth-
 519 quake cycle and Lake Bonneville. The transient viscosity inferred by *Pollitz* [2003] is constrained
 520 by the earliest phase of postseismic deformation following the Hector Mine earthquake. While
 521 *Pollitz* [2003] ruled out deep afterslip as an alternative mechanism based on inconsistent ver-
 522 tical deformation, it is still possible to successfully describe all components of early postseis-
 523 mic deformation following the Hector Mine earthquake with afterslip at seismogenic depths
 524 [*Jacobs et al.*, 2002]. It is then possible that the preferred rheologic model from *Pollitz* [2003]
 525 was biased towards inferring a particularly low transient viscosity by neglecting to account for
 526 afterslip. This is in contrast to the present study, where we have inferred a viscosity structure
 527 simultaneously with afterslip. We also argue that a transient rheology is necessary to explain
 528 postseismic deformation; however, our preferred transient viscosity of $\sim 10^{18}$ Pa s in the up-
 529 per mantle is an order of magnitude larger than the transient viscosity found by *Pollitz* [2003].
 530 Since a Zener model is able to describe the available postseismic deformation following the
 531 El Mayor-Cucapah earthquake, any Burgers rheology with a steady-state viscosity that is \gtrsim
 532 10^{20} Pa s, effectively infinite over five years, would also be able to describe the postseismic
 533 deformation. Such a Burgers model might then be consistent with the steady-state viscosities
 534 necessary for lake loading, interseismic deformation, and mantle dynamics.

535 5 Conclusion

536 We have extracted a filtered and smoothed estimate of postseismic deformation follow-
 537 ing the El Mayor-Cucapah earthquake from GPS displacement time series. We treated post-
 538 seismic deformation as a stochastic process where we did not presume any characteristic shape
 539 of the postseismic time series. Our estimated postseismic deformation reveals far-field (epi-
 540 central distances beyond ~ 200 km) transient deformation which is largely undetectable after
 541 about three years. Near-field deformation exhibits transience that decays to a sustained, ele-
 542 vated rate after about one or two years. We found that near-field transient deformation can be
 543 explained with shallow afterslip, and the sustained rate of near-field deformation can either
 544 be explained with continued afterslip or relaxation in a lower crustal with a viscosity of $\sim 10^{19}$
 545 Pa s. Far-field transient deformation can be more definitively ascribed to viscoelastic relax-
 546 ation at depths greater than ~ 60 km. Beneath that depth, a transient viscosity of $\sim 10^{18}$ Pa s
 547 is required to describe the rate of far-field deformation throughout the five years considered
 548 in this study. By describing the available postseismic deformation with a transient rheology
 549 in the mantle, our preferred model does not conflict with the generally higher steady-state vis-
 550 cosities inferred from geophysical processes occurring over longer time scales.

551 **Acknowledgements**

552 We thank Andy Freed for an illuminating discussion on the data used in this study. This
 553 material is based on EarthScope Plate Boundary Observatory data services provided by UN-
 554 AVCO through the GAGE Facility with support from the National Science Foundation (NSF)
 555 and National Aeronautics and Space Administration (NASA) under NSF Cooperative Agree-
 556 ment No. EAR-1261833. This material is based upon work supported by the National Science
 557 Foundation under Grant Numbers EAR 1045372 and EAR 1245263.

558 **References**

- 559 Aagaard, B. T., M. G. Knepley, and C. A. Williams (2013). A domain decomposition
 560 approach to implementing fault slip in finite-element models of quasi-static and dy-
 561 namic crustal deformation, *Journal of Geophysical Research: Solid Earth*, 118, doi:
 562 10.1002/jgrb.50217.
- 563 Argus, D. F., M. B. Heflin, G. Peltzer, F. Crampé, and F. H. Webb (2005), Interseismic
 564 strain accumulation and anthropogenic motion in metropolitan Los Angeles, *Journal of*
 565 *Geophysical Research: Solid Earth*, 110(4), 1–26, doi:10.1029/2003JB002934.
- 566 Aster, R. C., B. Borchers, and C. H. Thurber (2011), Parameter Estimation and Inverse
 567 Problems, vol. 90, Academic Press.
- 568 Bawden, G. W., W. Thatcher, R. S. Stein, K. W. Hudnut, and G. Peltzer (2001), Tectonic
 569 contraction across Los Angeles after removal of groundwater pumping effects., *Nature*,
 570 412(August), 812–815, doi:10.1038/35090558.
- 571 Bills, B. G., and G. M. May (1987), Lake Bonneville: Constraints on Lithospheric Thick-
 572 ness and Upper Mantle Viscosity From Isostatic Warping of Bonneville, Provo, and
 573 Gilbert Stage Shorelines, *Journal of Geophysical Research-Solid Earth and Planets*,
 574 92(B11), 11,493–11,508, doi:10.1029/JB092iB11p11493.
- 575 Çakir, Z., S. Ergintav, H. Özener, U. Dogan, A. M. Akoglu, M. Meghraoui, and
 576 R. Reilinger (2012), Onset of aseismic creep on major strike-slip faults, *Geology*,
 577 40(12), 1115–1118, doi:10.1130/G33522.1.
- 578 Cavalié, O., M. P. Doin, C. Lasserre, and P. Briole (2007), Ground motion measurement in
 579 the Lake Mead area, Nevada, by differential synthetic aperture radar interferometry time
 580 series analysis: Probing the lithosphere rheological structure, *Journal of Geophysical*
 581 *Research: Solid Earth*, 112(3), 1–18, doi:10.1029/2006JB004344.
- 582 Cetin, E., Z. Cakir, M. Meghraoui, S. Ergintav, and A. M. Akoglu (2014), Extent and
 583 distribution of aseismic slip on the Ismetpasa segment of the North Anatolian Fault
 584 (Turkey) from Persistent Scatterer InSAR, *Geochemistry, Geophysics, Geosystems*, 15,
 585 doi:10.1002/2014GC005307. Received.
- 586 Chopra, P. N. (1997), High-temperature transient creep in olivine rocks, *Tectonophysics*,
 587 279, 93–111, doi:10.1016/S0040-1951(97)00134-0.
- 588 Crittenden, M. (1967), Viscosity and Finite Strength of the Mantle as Determined from
 589 Water and Ice Loads*, *Geophysical Journal of the Royal Astronomical ...*, pp. 261–279,
 590 doi:10.1111/j.1365-246X.1967.tb06243.x.
- 591 Davis, J. L., B. P. Wernicke, and M. E. Tamisiea (2012), On seasonal signals in geode-
 592 tic time series, *Journal of Geophysical Research: Solid Earth*, 117(1), 1–10, doi:
 593 10.1029/2011JB008690.
- 594 Feigl, K. L., and W. Thatcher (2006), Geodetic observations of post-seismic transients in
 595 the context of the earthquake deformation cycle, *Comptes Rendus - Geoscience*, 338,
 596 1012–1028, doi:10.1016/j.crte.2006.06.006.
- 597 Fletcher, J. M., O. J. Teran, T. K. Rockwell, M. E. Osokin, K. W. Hudnut, K. J. Mueller,
 598 R. M. Spelz, S. O. Akciz, E. Masana, G. Faneros, E. J. Fielding, S. Leprince, A. E.
 599 Morelan, J. Stock, D. K. Lynch, A. J. Elliott, P. Gold, J. Liu-Zeng, A. González-
 600 Ortega, A. Hinojosa-Corona, and J. González-García (2014), Assembly of a large
 601 earthquake from a complex fault system: Surface rupture kinematics of the 4 April

- 602 2010 El Mayor-Cucapah (Mexico) Mw 7.2 earthquake, *Geosphere*, 10(4), 797–827,
603 doi:10.1130/GES00933.1.
- 604 Freed, A. M., R. Bürgmann, E. Calais, J. Freymueller, and S. Hreinsdóttir (2006), Implications
605 of deformation following the 2002 Denali, Alaska, earthquake for postseismic
606 relaxation processes and lithospheric rheology, *Journal of Geophysical Research: Solid
607 Earth*, 111, 1–23, doi:10.1029/2005JB003894.
- 608 Freed, A. M., R. Bürgmann, and T. Herring (2007), Far-reaching transient motions after
609 Mojave earthquakes require broad mantle flow beneath a strong crust, *Geophysical
610 Research Letters*, 34, 1–5, doi:10.1029/2007GL030959.
- 611 Gonzalez-Ortega, A., Y. Fialko, D. Sandwell, F. A. Nava-pichardo, J. Fletcher,
612 J. Gonzalez-garcia, B. Lipovsky, M. Floyd, and G. Funning (2014), El Mayor-
613 Cucapah (Mw7.2) earthquake: early near-field postseismic deformation from In-
614 Sar and GPS observations, *Journal of Geophysical Research*, 119, 1482–1497, doi:
615 10.1002/2013JB010193.Received.
- 616 Hauksson, E., J. Stock, K. Hutton, W. Yang, J. A. Vidal-Villegas, and H. Kanamori
617 (2011), The 2010 Mw 7.2 El mayor-cucapah earthquake sequence, Baja California
618 Mexico and Southernmost California, USA: Active seismotectonics along the
619 Mexican pacific margin, *Pure and Applied Geophysics*, 168(3918), 1255–1277, doi:
620 10.1007/s00024-010-0209-7.
- 621 Hearn, E. H. (2003), What can GPS data tell us about the dynamics of post-seismic defor-
622 mation ?, (2003), 753–777.
- 623 Hearn, E. H., S. McClusky, S. Ergintav, and R. E. Reilinger (2009), Izmit earthquake post-
624 seismic deformation and dynamics of the North Anatolian Fault Zone, *Journal of Geo-
625 physical Research: Solid Earth*, 114(August 2008), 1–21, doi:10.1029/2008JB006026.
- 626 Hetland, E. A. (2003), Postseismic relaxation across the Central Nevada Seismic Belt,
627 *Journal of Geophysical Research*, 108(Figure 2), 1–13, doi:10.1029/2002JB002257.
- 628 Hetland, E. A., and G. Zhang (2014), Effect of shear zones on post-seismic deformation
629 with application to the 1997 Mw 7.6 manyi earthquake, *Geophysical Journal Interna-
630 tional*, 198, 259–269, doi:10.1093/gji/ggu127.
- 631 Hines, T. T., and E. A. Hetland (2013), Bias in estimates of lithosphere viscosity from
632 interseismic deformation, *Geophysical Research Letters*, 40(16), 4260–4265, doi:
633 10.1002/grl.50839.
- 634 Hines, T. T., and E. A. Hetland (2016), Rapid and simultaneous estimation of fault slip
635 and heterogeneous lithospheric viscosity from post-seismic deformation, *Geophysical
636 Journal International*, 204(1), 569–582, doi:10.1093/gji/ggv477.
- 637 Jacobs, A., D. Sandwell, Y. Fialko, and L. Sichoux (2002), The 1999 (Mw7.1) Hector
638 Mine, California, Earthquake: Near-Field Postseismic Deformation from ERS Interfer-
639 ometry, *Bulletin of the Seismological Society of America*, 92(May), 1433–1442.
- 640 Johnson, K. M., and P. Segall (2004), Viscoelastic earthquake cycle models with deep
641 stress-driven creep along the San Andreas fault system, *Journal of Geophysical Research
642 B: Solid Earth*, 109, 1–19, doi:10.1029/2004JB003096.
- 643 Johnson, K. M., R. Bürgmann, and J. T. Freymueller (2009), Coupled afterslip and vis-
644 coelastic flow following the 2002 Denali Fault, Alaska earthquake, *Geophysical Journal
645 International*, 176(3), 670–682, doi:10.1111/j.1365-246X.2008.04029.x.
- 646 Jónsson, S., P. Segall, R. Pedersen, and G. Bjornsson (2003), Post-earthquake ground
647 movements correlated to pore-pressure transients, *Nature*, 424(July), 179–183, doi:
648 10.1038/nature01758.1.
- 649 Kaufmann, G., and F. Amelung (2000), Reservoir-induced deformation and continental
650 rheology in vicinity of Lake Mead, Nevada, *Journal of Geophysical Research*, 105(B7),
651 16,341, doi:10.1029/2000JB900079.
- 652 Kroll, K. A., E. S. Cochran, K. B. Richards-Dinger, and D. F. Sumy (2013), Aftershocks
653 of the 2010 Mw 7.2 El Mayor-Cucapah earthquake reveal complex faulting in the Yuha
654 Desert, California, *Journal of Geophysical Research: Solid Earth*, 118(October), 6146–
655 6164, doi:10.1002/2013JB010529.

- 656 Lekic, V., S. W. French, and K. M. Fischer (2011), Lithospheric Thinning Beneath Rifted
 657 Regions of Southern California, *Science*, 334(November), 783–787.
- 658 Liu, H.-P., D. L. Anderson, and H. Kanamori (1976), Velocity dispersion due to anelasticity; implications for seismology and mantle composition, *Geophysical Journal International*, 47(1), 41–58, doi:10.1111/j.1365-246X.1976.tb01261.x.
- 661 Lundgren, P., E. A. Hetland, Z. Liu, and E. J. Fielding (2009), Southern San Andreas-San
 662 Jacinto fault system slip rates estimated from earthquake cycle models constrained by
 663 GPS and interferometric synthetic aperture radar observations, *Journal of Geophysical
 664 Research: Solid Earth*, 114(2), 1–18, doi:10.1029/2008JB005996.
- 665 McGuire, J. J., and P. Segall (2003), Imaging of aseismic fault slip transients recorded
 666 by dense geodetic networks, *Geophysical Journal International*, 155(3), 778–788, doi:
 667 10.1111/j.1365-246X.2003.02022.x.
- 668 Meade, B. J., and B. H. Hager (2005), Block models of crustal motion in southern Cal-
 669 ifornia constrained by GPS measurements, *Journal of Geophysical Research B: Solid
 670 Earth*, 110, 1–19, doi:10.1029/2004JB003209.
- 671 Murray, J. R., and P. Segall (2005), Spatiotemporal evolution of a transient slip event on
 672 the San Andreas fault near Parkfield, California, *Journal of Geophysical Research : Solid
 673 Earth*, 110(9), 1–12, doi:10.1029/2005JB003651.
- 674 Nur, A., and G. Mavko (1974), Postseismic viscoelastic rebound, *Science*, 183(4121),
 675 204–206, doi:10.1038/098448b0.
- 676 O'Connell, R. J. (1971), Rheology of the Mantle, *EOS, Transactions, American Geophysical Union*, 52, 140–142.
- 677 Oskin, M. E., J. R. Arrowsmith, A. Hinojosa Corona, A. J. Elliott, J. M. Fletcher, E. J.
 678 Fielding, P. O. Gold, J. J. Gonzalez Garcia, K. W. Hudnut, J. Liu-Zeng, and O. J. Teran
 680 (2012), Near-field deformation from the El Mayor-Cucapah earthquake revealed by
 681 differential LIDAR, *Science*, 335(6069), 702–705, doi:10.1126/science.1213778.
- 682 Pollitz, F., C. Wicks, and W. Thatcher (2001), Mantle Flow Beneath a Continental Strike-
 683 Slip Fault : Postseismic Deformation After the 1999 Hector Mine Earthquake, *Science*,
 684 1814(2001), 1814–1818, doi:10.1126/science.1061361.
- 685 Pollitz, F. F. (2003), Transient rheology of the uppermost mantle beneath the Mo-
 686 jave Desert, California, *Earth and Planetary Science Letters*, 215, 89–104, doi:
 687 10.1016/S0012-821X(03)00432-1.
- 688 Pollitz, F. F., G. Peltzer, and R. Bürgmann (2000), Mobility of continental mantle: Evi-
 689 dence from postseismic geodetic observations following the 1992 Landers earthquake,
 690 *Journal of Geophysical Research*, 105(1999), 8035, doi:10.1029/1999JB900380.
- 691 Pollitz, F. F., R. Bürgmann, and W. Thatcher (2012), Illumination of rheological mantle
 692 heterogeneity by the M7.2 2010 El Mayor-Cucapah earthquake, *Geochemistry, Geo-
 693 physics, Geosystems*, 13(6), 1–17, doi:10.1029/2012GC004139.
- 694 Rauch, H. E., F. Tung, and C. T. Striebel (1965), Maximum likelihood estimates of linear
 695 dynamic systems, *AIAA Journal*, 3(8), 1445–1450.
- 696 Riva, R. E. M., and R. Govers (2009), Relating viscosities from postseismic relaxation to
 697 a realistic viscosity structure for the lithosphere, *Geophysical Journal International*, 176,
 698 614–624, doi:10.1111/j.1365-246X.2008.04004.x.
- 699 Rollins, C., S. Barbot, and J.-P. Avouac (2015), Postseismic Deformation Following the
 700 2010 M7.2 El Mayor-Cucapah Earthquake : Observations , Kinematic Inversions , and
 701 Dynamic Models, *Pure and Applied Geophysics*, doi:10.1007/s00024-014-1005-6.
- 702 Savage, J. C. (1990), Equivalent strike-slip earthquake cycles in half-space and
 703 lithosphere-asthenosphere earth models, *Journal of Geophysical Research*, 95, 4873,
 704 doi:10.1029/JB095iB04p04873.
- 705 Savage, J. C., and J. L. Svart (2009), Postseismic relaxation following the 1992 M 7.3
 706 Landers and 1999 M 7.1 Hector Mine earthquakes , southern California, *Journal of
 707 Geophysical Research*, 114(B01401), doi:10.1029/2008JB005938.
- 708 Savage, J. C., J. L. Svart, and S. B. Yu (2005), Postseismic relaxation and transient creep,
 709 *Journal of Geophysical Research: Solid Earth*, 110, 1–14, doi:10.1029/2005JB003687.

- 710 Segall, P., and M. Mathews (1997), Time dependent inversion of geodetic data, *Journal of
Geophysical Research*, 102.
- 711
- 712 Spinler, J. C., R. A. Bennett, C. Walls, L. Shawn, and J. J. G. Garcia (2015), Assessing long-term postseismic deformation following the M7.2 4 April 2010, El
713 Mayor-Cucapah earthquake with implications for lithospheric rheology in the
714 Salton Trough, *Journal of Geophysical Research: Solid Earth*, 120, 3664–3679, doi:
715 10.1002/2014JB011613.Received.
- 716
- 717 Wei, M., D. Sandwell, Y. Fialko, and R. Bilham (2011a), Slip on faults in the Imperial
718 Valley triggered by the 4 April 2010 Mw 7.2 El Mayor-Cucapah earthquake revealed by
719 InSAR, *Geophysical Research Letters*, 38(January), 1–6, doi:10.1029/2010GL045235.
- 720
- 721 Wei, M., Y. Liu, Y. Kaneko, J. J. McGuire, and R. Bilham (2015), Dynamic triggering of
722 creep events in the Salton Trough, Southern California by regional M5.4 earthquakes
723 constrained by geodetic observations and numerical simulations, *Earth and Planetary
Science Letters*, 427, 1–10, doi:10.1016/j.epsl.2015.06.044.
- 724
- 725 Wei, S., E. Fielding, S. Leprince, A. Sladen, J.-P. Avouac, D. Helmberger, E. Hauksson,
726 R. Chu, M. Simons, K. Hudnut, T. Herring, and R. Briggs (2011b), Superficial sim-
727 plicity of the 2010 El MayorCucapah earthquake of Baja California in Mexico, *Nature
Geoscience*, 4(9), 615–618, doi:10.1038/ngeo1213.
- 728
- 729 Yang M., and M. N. Toksöz (1981), Time-dependent deformation and stress relaxation
730 after strike-slip earthquakes, *Journal of Geophysical Research*, 86, 2889–2901.
- 731
- 732 Yuen, D. A., and W. R. Peltier (1982), Normal modes of the viscoelastic earth, *Geo-
physical Journal of the Royal Astronomical Society*, 69, 495–526, doi:10.1111/j.1365-
246X.1982.tb04962.x.